High-Speed Stress Field Measurement In A Soft Substrate During Droplet Impact

Yuto Yokoyama[1,2], Hirokazu Maruoka[3,4], Sayaka Ichihara[2], Yoshiyuki Tagawa[2,*]

1: Micro/Bio/Nanofluidics Unit, Okinawa Institute of Science and Technology, Japan
2: Dept. of Mechanical Systems Engineering, Tokyo University of Agriculture and Technology, Japan
3: Nonlinear and Non-equilibrium Physics Unit, Okinawa Institute of Science and Technology, Japan
4: Yukawa Institute for Theoretical Physics, Kyoto University, Japan
*Corresponding author: tagawayo@cc.tuat.ac.jp

Keywords: Stress Field Measurement, High-Speed Photoelastic Tomography, Droplet Impact, Soft Material.

ABSTRACT

In this study, we utilized high-speed photoelastic tomography to quantify dynamic stress fields within a soft substrate during droplet impact. This manuscript details the measurement technique, which employs a high-speed polarization camera and the principles of photoelastic tomography. Our method successfully enabled the quantitative measurement of dynamic stress fields in a soft substrate during droplet impact. Additionally, we conducted an analysis of the impact force derived through the spatial integration of the measured stress field. The discussion explored the interplay between the maximum impact force, droplet viscosity, and substrate elasticity. Our findings indicate that the maximum impact force $F_{\max}$ can be expressed as a function with a self-similar variable of Re/Ca^2, where Re is Reynolds number representing the droplet inertial force and droplet viscous force and Ca is Cauchy number representing the ratio of the droplet inertial force and substrate elastic force. This combination, Re/Ca^2, represents the relationship between the relaxation time of droplet and substrate deformation (η/E), the contact time of the droplet (R/V), and the ratio of substrate elastic force to droplet inertial force. Consequently, the maximum impact force $F_{\max}$ is determined by the balance between the relaxation and contact times. We believe that our developed method will significantly enhance the understanding of droplet impact phenomena. Furthermore, it holds potential for broader applications in various engineering processes, such as analyzing stress distribution in materials caused by liquid jet impact and studying cavitation bubbles in viscoelastic materials. This method's ability to provide detailed quantitative measurements of dynamic stress fields offers a valuable tool for future research and technological advancements in related fields.

1. Introduction

Droplet impact phenomena are essential in various industrial processes, such as inkjet printing (Lohse, 2022) and spray cooling (Liang & Mudawar, 2017; Breitenbach et al., 2018), and their prediction and control are required. In particular, the maximum expansion radius after impact and

splash phenomena affect the quality and efficiency of these technologies and have been the subject of many studies (Yarin, 2006; Josserand & Thoroddsen, 2016). On the other hand, relatively few studies have focused on the forces and stresses acting on the substrate side during impact (Cheng et al., 2022). This is important for technologies such as water cutters (Mitchell et al., 2019b) and needle-free injection using liquid jets (Miyazaki et al., 2021). Understanding the stress field in the substrate during droplet impact is also academically significant as it reveals aspects of droplet behavior that may not be captured through conventional high-speed imaging. For example, it can unveil the development of a viscous boundary layer within the droplet and provide insights into the impact behavior at very short timescales immediately after impact.

Previous studies have primarily concentrated on the normal substrate impact force generated during droplet impact (Zhang et al., 2017; Gordillo et al., 2018; Mitchell et al., 2019a), as it can be easily measured using a piezoelectric sensor. However, experimental measurement of the stress distribution generated by an impacting droplet with high spatio-temporal resolutions is more difficult than measuring the impact force and has rarely been performed. Very recently, Sun et al. (T.-P. Sun et al., 2022) have used digital image correlation to quantify the deformation of elastic gels due to droplet impact, thereby realizing high-speed measurement of the stress distribution caused by droplet impact. This provided experimental evidence of the theoretically predicted stress distribution by Philippi et al. (2016). Nevertheless, methods for quantitative measurement of the stress distribution during droplet impact at high spatio-temporal resolution are still lacking. In addition to the above method, new stress measurement methods must be developed to not only validate theoretical and numerical predictions but also to perform systematic experiments over a range of untested parameters.

Photoelastic tomography can quantitatively evaluate the stress field of such phenomena. Photoelasticity tomography developed as a method for measuring residual stress in glass and has mainly been used to measure the static stress field in hard materials (Frocht, 1941; H. Aben & Guillemet, 1993; Asai et al., 2019; Ramesh & Ramakrishnan, 2016). This method evaluates the stress field by measuring photoelastic parameters due to the optical anisotropy (birefringence) inside a material caused by stress loading using polarized light (H. Aben & Guillemet, 1993). The recent development of high-speed polarization cameras (Onuma & Otani, 2014) has expanded the applicability of this method to dynamic fields (Miyazaki et al., 2021). The high-speed polarization camera can visualize dynamic stress fields and measure photoelastic parameters in soft materials, but it has not been used for quantitative stress measurement through photoelastic tomography. In contrast, we recently developed a high-speed stress field measurement in a soft substrate using photoelastic tomography (Yokoyama et al., 2024). Consequently, a wide range of stress fields from $\mathcal{O}(10^{-1})$ to $\mathcal{O}(10^{1})$ kPa were measured simultaneously with large deformation of the substrate.

In this study, we applied this high-speed photoelastic tomography to measure dynamic stress fields in a soft material during droplet impact. In this manuscript, the measurement method us-

ing a high-speed polarization camera and the principle of photoelastic tomography will be described based on our recent paper (Yokoyama et al., 2024). Additionally, the impact force obtained by spatially integrating the measured stress field was analyzed, and the relationship between its maximum value, droplet viscosity, and substrate elasticity was discussed.

2. Method

2.1. Experiment

The schematic of the experimental setup used in this study is shown in Fig. 1. In the experiment, a high-speed polarization camera (CRYSTA PI-1P, Photron, 20,000 fps), a soft substrate (polyurethane gel phantom, Exseal Co., Ltd., modulus 47.4 kPa), and a light source producing circularly polarized light were placed in a straight line. A solid sphere or droplet was impacted on a soft substrate. The z axis is the central axis of the solid sphere and droplet, and $z = 0$ is the surface of the substrate. The r-axis is parallel to the z-axis, and $r = 0$ is defined as the intersection point with the z-axis. Silicone oil (Shin-Etsu) with viscosities of $10^0, 10^1, 10^2, 10^3, 10^4$ cSt was used as a droplet. The average droplet radius R was 1.27 mm. Plastic spheres with radius $R = 2.98$ mm and density $\rho = 997.3\,\mathrm{kg/m^3}$ were used as solid spheres. Impact velocities V of the solid spheres and droplets were varied between $0.2 \sim 3.0\,\mathrm{m/s}$ by adjusting their falling heights.

Photoelasticity measures the photoelastic parameters of a material using polarized light to evaluate the stress field due to optical anisotropy (birefringence) caused by stress loading (H. Aben & Guillemet, 1993). When circularly polarized light from a light source enters a material under stress, it is emitted as elliptically polarized light with photoelastic parameters (phase retardation Δ and orientation ϕ) corresponding to the stress state in the material. It is possible to measure both the retardation Δ orientation ϕ of light emitted by using the polarization camera. Four linear polarizers are installed in neighboring pixels of the image sensor of the polarization camera. The angles of the polarizers are $0°$, $45°$, $90°$, and $135°$. The camera's sensor measures light intensity values through linear polarizers, denoted by $I_{0°}, I_{45°}, I_{90°}$, and $I_{135°}$. By using the four-step phase-shifting method (Ramesh, 2021; Otani et al., 1994; Onuma & Otani, 2014; Yokoyama et al., 2023), Δ and ϕ can be obtained from the four intensity values as follows:

$$\Delta = \frac{\lambda}{2\pi} \sin^{-1} \frac{\sqrt{(I_{90°} - I_{0°})^2 + (I_{45°} - I_{135°})^2}}{I/2}, \tag{1}$$

$$\phi = \frac{1}{2} \tan^{-1} \frac{I_{90°} - I_{0°}}{I_{45°} - I_{135°}}, \tag{2}$$

where $I = I_{0°} + I_{45°} + I_{90°} + I_{135°}$. Δ and ϕ are calculated by a software (Photron Ltd, CRYSTA Stress Viewer).

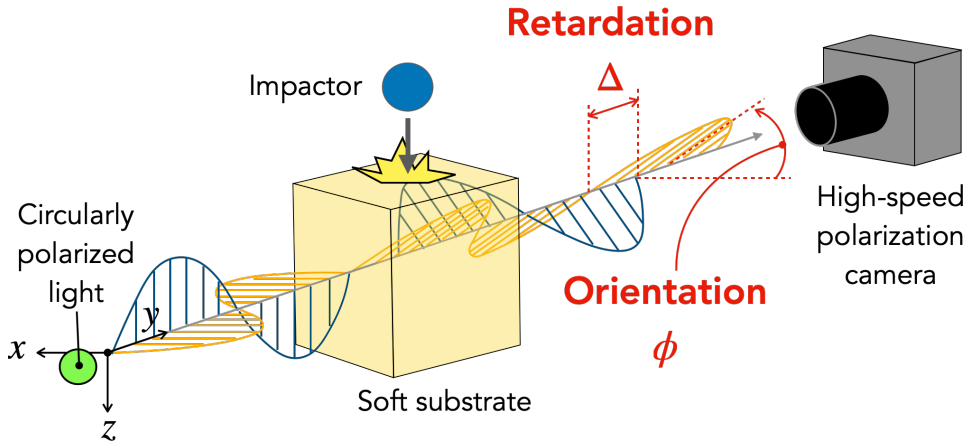

Figure 1. Experimental setup for measuring the stress field in a soft substrate during a sphere or droplet impact.

2.2. Photoelstic tomography

There are the following relationships between the stress field inside a material and measured photoelastic parameters (H. Aben & Puro, 1997; Doyle, 1982; H. Aben et al., 2010b):

$$V_1 \equiv \Delta \cos 2\phi = C \int_{-\infty}^{\infty} (\sigma_{xx} - \sigma_{zz})\, dy, \tag{3}$$

$$V_2 \equiv \Delta \sin 2\phi = 2C \int_{-\infty}^{\infty} \sigma_{xz} dy, \tag{4}$$

where C is the material-specific stress-optic coefficient, and σ_{xx}, σ_{zz}, and σ_{xz} are the stress components in Cartesian coordinates, with the y-axis as the camera's optical axis.

As shown by the integrated equations, the photoelastic parameters that can be measured using a polarization camera are the integrated values of the internal stress field along the camera's optical axis. Therefore, tomography is required to convert the photoelastic parameters into the stress tensor components at each point inside the material. H. Aben & Errapart (2012) suggested that the problem of stress field tomography could be solved if it could be reduced to a problem of scalar field tomography for a single stress tensor component. To determine the stress field inside a material using photoelastic tomography, it is necessary to measure the photoelastic parameters in two sections, the upper section and lower section, parallel to the x-y plane and separated by a distance Δz (H. K. Aben et al., 1992; H. Aben et al., 2008). It's usually recommended to measure the camera's optical axis in multiple directions around the z-axis to ensure precise measurements. We now consider an arbitrary three-dimensional stress field with boundaries (see Fig. 2(a)). In a part of this field, which is indicated by the element ABX in Fig. 2(b), the force equilibrium along the x-axis can be written as following equations:

$$\Delta z \int_{B}^{A} \sigma_{xx} dy = T_u - T_l, \tag{5}$$

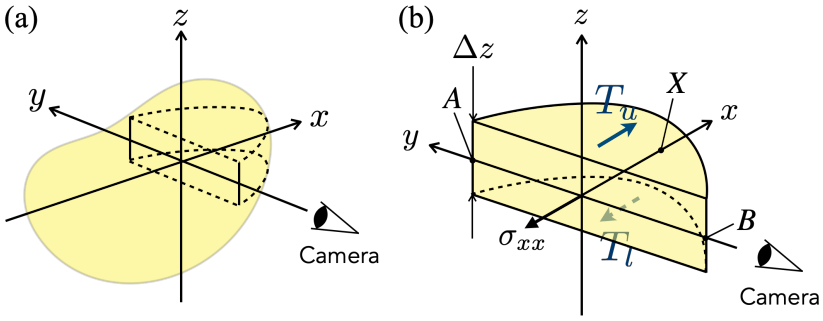

Figure 2. (a) A general three-dimensional stress field. (b) The considered element ABX enclosed by the dashed line.

where T_u and T_l are shear forces on the upper and lower surfaces of the element and A, B denote the boundary of the three-dimensional stress field on the y-axis. T_u and T_l can be written using Eq. (4):

$$T_u = \frac{1}{2C}\int_x^{X'} V_2' dx, \quad T_l = \frac{1}{2C}\int_x^{X} V_2 dx. \tag{6}$$
$$\because\ T_l = \int_x^X \int_A^B \sigma_{xz} dy dx = \int_x^X \frac{1}{2C} V_2 dx$$

Here, V_2' is the V_2 measured in the upper section. X' and X are the outer positions of the upper and lower sections, respectively. Substituting Eqs. (5) and (6) into Eqs. (3) and (4), we get

$$\int_B^A \sigma_{xz} dy = \frac{1}{2C} V_2, \tag{7}$$

$$\int_B^A \sigma_{zz} dy = \frac{1}{2C\Delta z}\left(\int_x^X V_2' dx - \int_x^X V_2 dx\right) - \frac{V_1}{C}. \tag{8}$$

If the stress field is axisymmetric, such as droplet impact, the stress field can be experimentally determined using Eqs. (7) and (8) (Anton et al., 2008; Errapart, 2011). In the case of an axisymmetric stress field, the stress tensor has four components: radial stress σ_{rr}, hoop stress $\sigma_{\theta\theta}$, axial stress σ_{zz}, and shear stresses σ_{rz}. The r-z plane is perpendicular to the camera's optical axis, and the z-axis is the axis of symmetry. To calculate the components σ_{rz} and σ_{zz}, we use the integrated relationships, Eqs. (7) and (8), using the measured values of Δ and ϕ. The equations of the theory of linear elasticity are used to reconstruct σ_{rr} and $\sigma_{\theta\theta}$ using calculated values of σ_{rz} and σ_{zz} (Errapart, 2011).

2.2.1. Determination of the shear and axial stresses

The shear and axial stresses, σ_{rz} and σ_{zz} can be determined from the photoelastic parameters using Eq. (4) based on the onion-peeling (OP) method (Anton et al., 2008). The OP method is one of the algorithms for numerically solving the inverse Abel transform, a well-known axisymmetric scalar field tomography method (Dasch, 1992; Xiong et al., 2020). The onion-peeling method models

the axisymmetric field as N rings (Fig. 3), each with a fixed scalar value and thickness of Δr. Integrated values measured by the polarization camera, $V_1^{(i)}$ and $V_2^{(i)}$ at a certain optical path, are the sum of the stresses acting on each ring along the length of the optical path $W_{i,j}$. For example, the relationship between an integrated value and shear stress acting on the ith ring, $V_2^{(i)}$ and $\sigma_{rz}^{(i)}$, respectively, can be described based on Eq. (7) as the following equation:

$$V_2^{(i)} = 4C \sum_{j=i}^{N} W_{i,j} \sigma_{xz}^{(j)} = 4C \sum_{j=i}^{N} W_{i,j} \sigma_{rz}^{(j)} \cos\theta_{i,j}, \tag{9}$$

where

$$W_{i,j} = \begin{cases} 0 & j < i, \\ \frac{\Delta r}{2}\sqrt{(2j+i)^2 - 4i^2} & j = i, \\ \frac{\Delta r}{2}\sqrt{(2j+i)^2 - 4i^2} - \frac{\Delta x}{2}\sqrt{(2j-i)^2 - 4i^2} & j > i, \end{cases} \tag{10}$$

and

$$\theta_{i,j} = \begin{cases} 0 & j = i, \\ \cos^{-1}\dfrac{2i}{2j-1} & j > i. \end{cases} \tag{11}$$

The stress values can be computed starting from the outermost ring and progressing inward, utilizing Eqs. (9) and (12). This allows us to determine the shear and axial stresses for all the rings. Note that the shear stress σ_{rz} is not axisymmetric when distributed in Cartesian coordinates' x-y plane, thus $\sigma_{xz} = \sigma_{rz}\cos\theta$. This is because photoelasticity can only measure the stress component projected onto the plane perpendicular to the camera's optical axis (Anton et al., 2008).

Similarly, the axial stress acting on the ith ring, $\sigma_{zz}^{(i)}$, can be determined using the following equation based on Eq. (8).

$$V_1^{(i)} - \frac{1}{2\Delta z}\sum_{j=1}^{i}(V_2'^{(j)} - V_2^{(j)})\Delta x = 2C\sum_{j=1}^{i} W_{i,j}\sigma_{zz}^{(j)} \tag{12}$$

2.2.2. Determination of the radial and hoop stresses

The equations of linear elasticity are used to determine the radial and stresses, σ_{rr} and $\sigma_{\theta\theta}$, as noted in (Errapart, 2011; H. Aben et al., 2010a). These stresses must satisfy both the equilibrium and compatibility equations,

$$\frac{\partial\sigma_{rr}}{\partial r} + \frac{\sigma_{rr} - \sigma_{\theta\theta}}{r} + \frac{\partial\sigma_{rz}}{\partial z} = 0, \tag{13}$$

$$\frac{\partial}{\partial r}\{\sigma_{\theta\theta} - \nu(\sigma_{rr} + \sigma_{zz})\} - (1+\nu)\frac{\sigma_{rr} - \sigma_{\theta\theta}}{r} = 0, \tag{14}$$

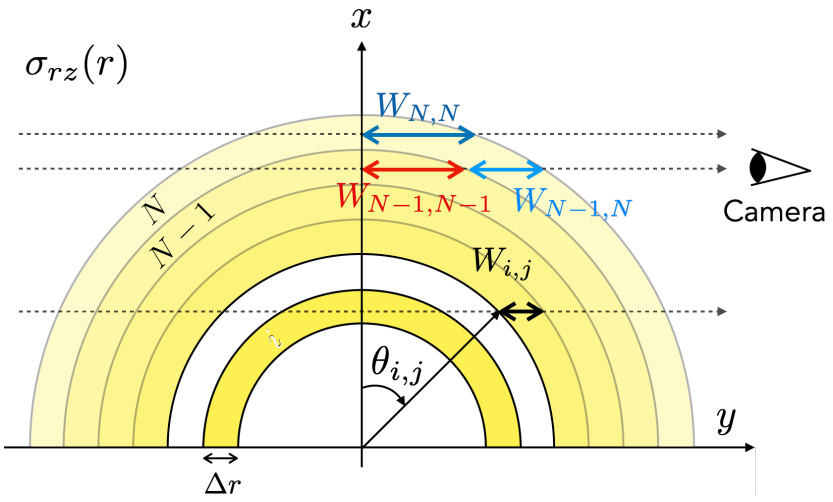

Figure 3. Diagram of onion-peeling algorithm.

respectively. The differential equations for σ_{rr} and $\sigma_{\theta\theta}$ can be obtained by transforming these equations as follows:

$$\frac{\partial \sigma_{rr}}{\partial r} = -\frac{\sigma_{rr} - \sigma_{\theta\theta}}{r} - \frac{\partial \sigma_{rz}}{\partial z}, \tag{15}$$

$$\frac{\partial \sigma_{\theta\theta}}{\partial r} = \frac{\sigma_{rr} - \sigma_{\theta\theta}}{r} - \nu\frac{\partial \sigma_{rz}}{\partial z} + \nu\frac{\partial \sigma_{zz}}{\partial r}. \tag{16}$$

The second and subsequent terms on the right-hand side of these equations are known values because they could be obtained by Eqs. (9) and (12). By numerically solving these differential equations, it is possible to determine both the radial and hoop stresses.

2.2.3. Quasi-static approximation

In the earlier sections, the tomography algorithm assumed equilibrium, except when it came to reconstructing the shear stress σ_{rz}. Therefore, to reconstruct stresses from the time-series data of the measured photoelastic parameters, we need to adopt the quasi-static approximation. We compare the impact velocity V and the pressure wave speed v_p in the material to confirm this approximation. The speed of the pressure wave v_p can be estimated using the following equation (Johnson, 1985):

$$v_p = \sqrt{E/\rho_s}, \tag{17}$$

where E and ρ_s are Young's modulus and the density of the substrate material, respectively. In cases of low-velocity impacts, where the impact velocity V is less enough than the pressure wave velocity v_p, the possibility of the quasi-static approximation being applicable is higher. In our experimental setup, the highest value observed for V/v_p is approximately 0.45. This arises from a maximum V of $3.0\,\mathrm{m/s}$ and an estimated v_p of $6.7\,\mathrm{m/s}$, with material properties E at $47.4\,\mathrm{kPa}$

and ρ_s at $1064\,\mathrm{kg/m^3}$. Consequently, we made the assumption that the quasi-static approximation remains valid in our experiment, given that the ratio V/v_p is below 1.

2.2.4. Validation of photoelastic tomography for a dynamic stress field measurement in a soft material

We carefully validated the applicability of photoelastic tomography to a dynamic stress field measurement in a soft material in our recent paper (Yokoyama et al., 2024). The investigation carried out in the paper contains both Hertzian contact and impact problems. When the external force and other contact conditions are known in advance, it becomes possible to theoretically derive the stress field within the material or the impact forces exerted on the material surface based on the Hertizan contact theory (Johnson, 1985; Ike, 2019; Love, 1929; Pradipto & Hayakawa, 2021; Kuwabara & Kono, 1987). This provides a means to assess the reliability of the experimentally reconstructed stress field obtained from photoelastic parameters.

Consequently, it was indicated that photoelastic tomography could measure all axisymmetric stress components in a soft substrate accurately. Even in the dynamic stress field, it was demonstrated that photoelastic tomography can be employed for the quantitative measurement of shear and axial stress waves. The details of the validation and its results are explained in (Yokoyama et al., 2024).

3. Results and discussion

3.1. Dynamic stress field measurement

Fig. 4 shows a solid sphere or droplets of different viscosities impacting a soft substrate at an impact velocity of approximately $2.8\,\mathrm{m/s}$. The time when the droplet and the solid sphere touched the substrate is defined as $0\,\mathrm{s}$. The lower part of each image shows the distributions of Δ and ϕ. The color bar in the figure indicates Δ, and the white arrow indicates ϕ.

In the case of droplets, the maximum retardation is observed approximately $0.2\,\mathrm{ms}$ after the impact, gradually decreasing over a longer time until it finally reaches $0\,\mathrm{nm}$. The maximum retardation increases as the droplet viscosity increases. The orientation is distributed radially from the origin of droplet impact, $(r, z) = (0, 0)$. From the retardation and orientation data, the stress field in the substrate can be reconstructed using the photoelastic tomography algorithm described in the previous section.

Here, we show the spatio-temporal distributions of axial and shear stresses as examples of stress field reconstruction results using photoelastic tomography. Figs. 5 and 6 show the reconstructed axial stress σ_{zz} and shear stress σ_{rz} obtained from the data of the photoelastic parameters (Fig. 4).

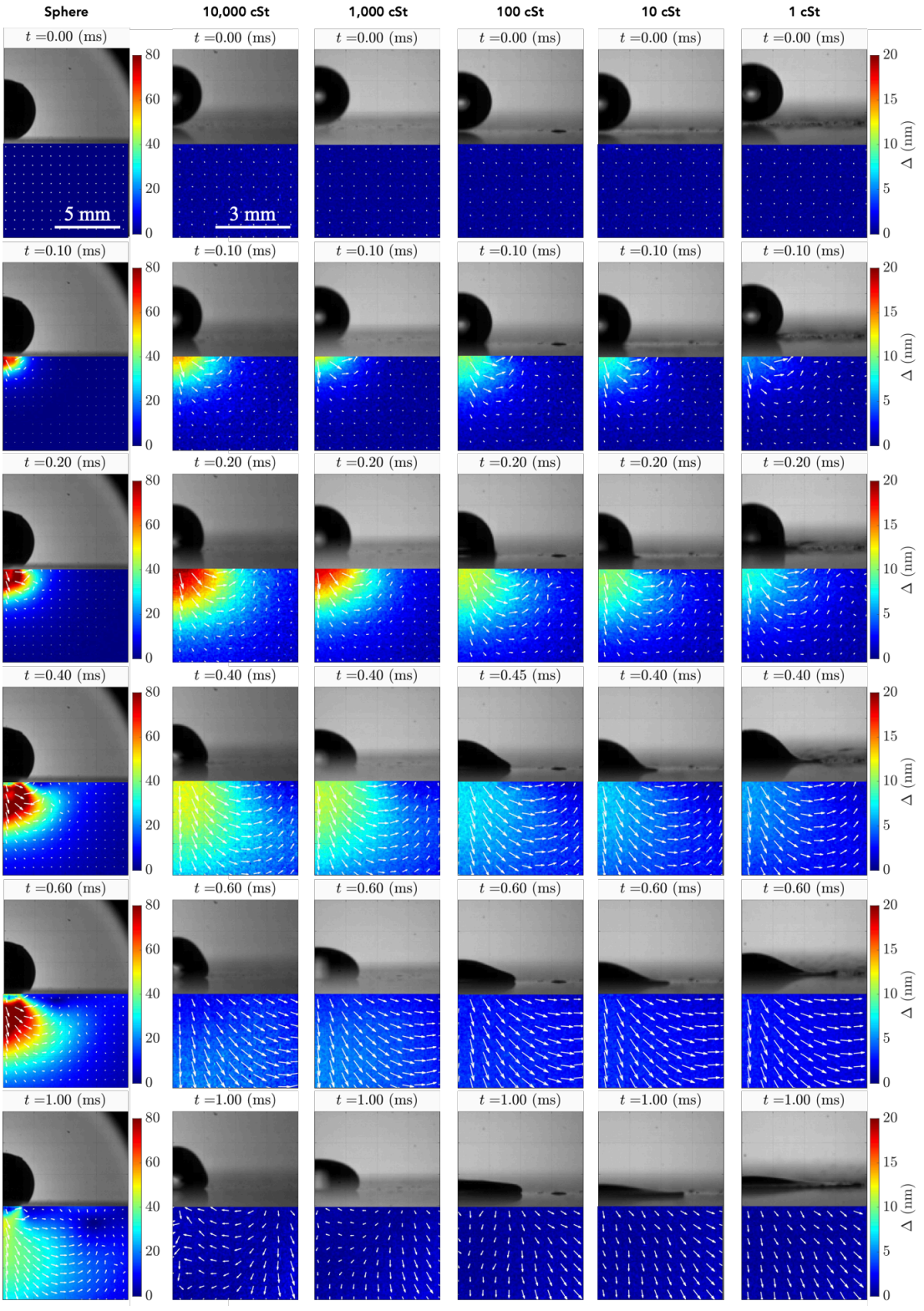

Figure 4. Spatio-temporal distribution of retardation (color) and orientation (white arrows) during a sphere and droplets impacting on a soft substrate when $V \simeq 2.8 \pm 0.1$ m/s.

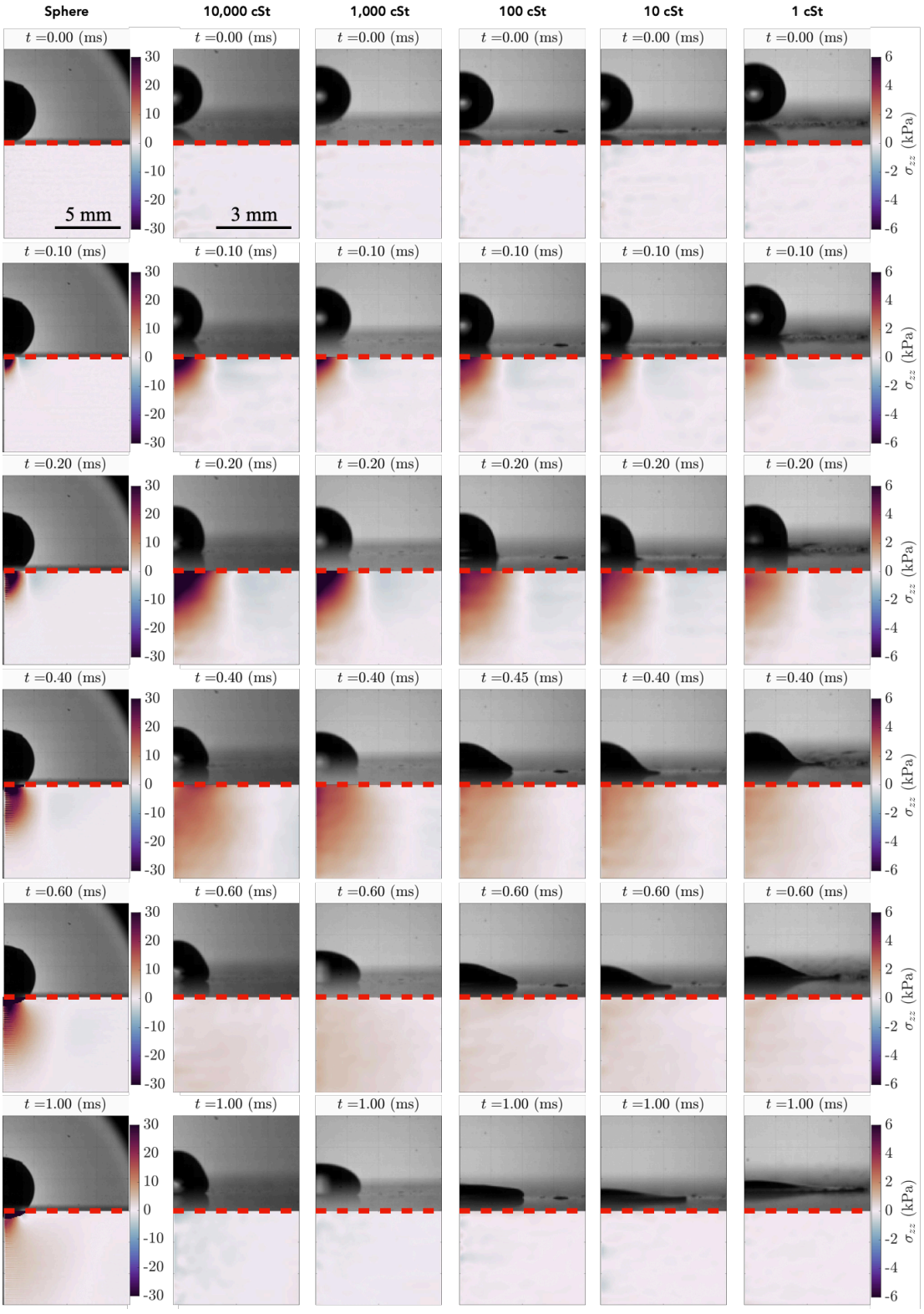

Figure 5. Spatio-temporal distribution of axial stress σ_{zz} during a sphere and droplets impacting on a soft substrate when $V \simeq 2.8 \pm 0.1$ m/s.

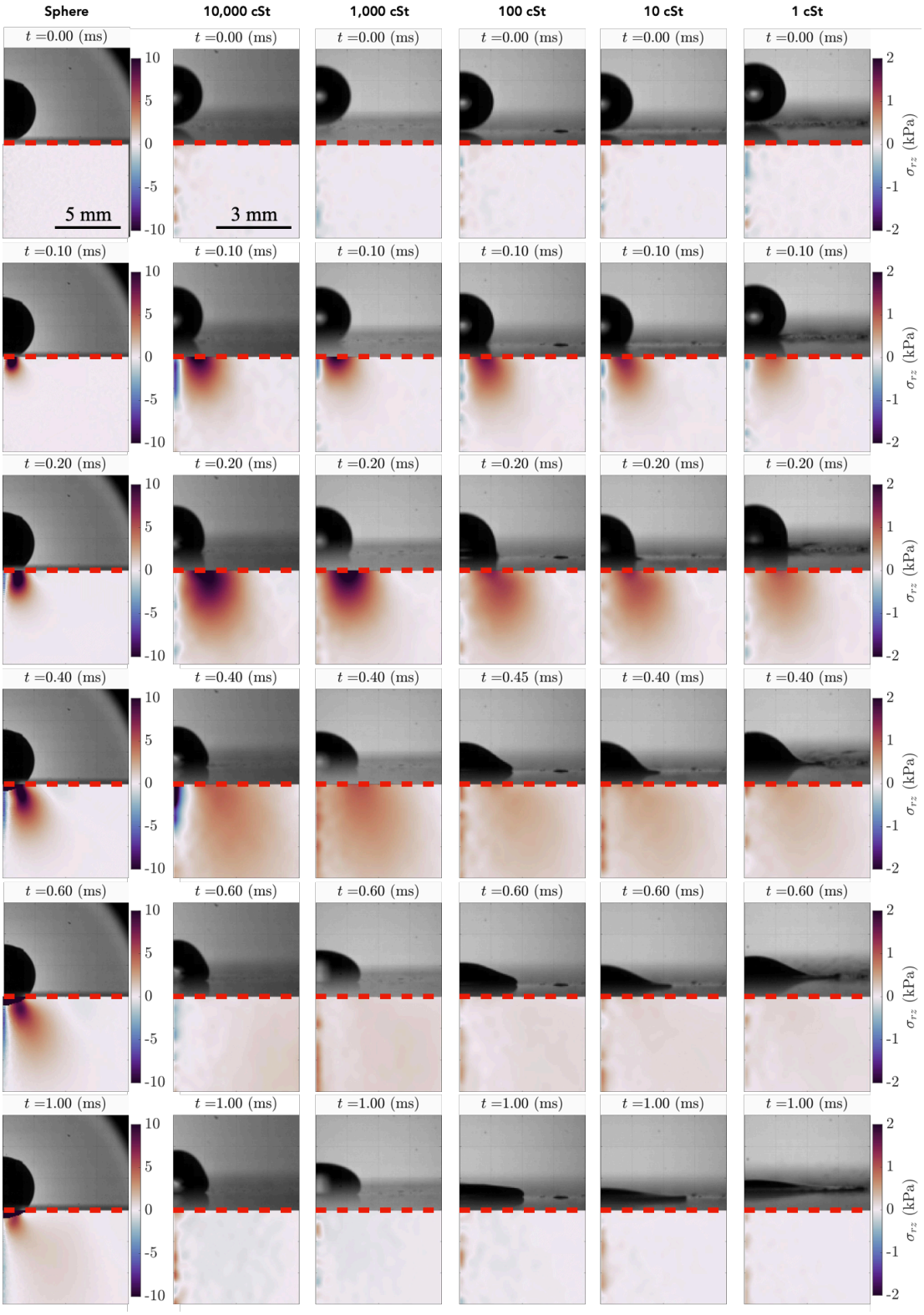

Figure 6. Spatio-temporal distribution of shear stress σ_{rz} during a sphere and droplets impacting on a soft substrate when $V \simeq 2.8 \pm 0.1$ m/s.

Focusing on the distribution along the z-axis of σ_{zz}, immediately after the collision, around $0.1\,\mathrm{ms}$, a region of high-stress concentration is observed near the contact interface between the droplet and the substrate. Subsequently, with the z-axis motion of the droplet, the stress propagates and decreases in the z-direction. Examining the distribution along the r-axis of σ_{zz}, in the region near the contact interface between the droplet and the substrate, positive values are indicated, while in the outer region, negative values are observed. The boundary between positive and negative stresses, initially following the periphery of the contact interface $r = a(t)$ immediately after the collision, propagates and decays in the r-direction beyond $r = a(t)$. Focusing on the distribution along the r-axis of σ_{rz}, around 0.1 ms after the collision, a region of high-stress concentration is observed near the periphery of the contact interface $r = a(t)$ between the droplet and the substrate. Subsequently, with the r-axis motion of the droplet, the stress propagates and decreases in the r-direction. This trend is consistent with the experimental measurements by Y. Sun et al. (2022) and the theoretical predictions by Philippi et al. (2016). These results indicate that photoelastic tomography can be used for dynamic stress field measurement in a soft substrate during droplet impact. Here, the negative value of the σ_{rz} along the z-axis is due to the measurement error of the orientation data. Theoretically, the orientation on the right side of the z-axis should be positive under our experimental condition. However, it shows sometimes the negative value near the z-axis, resulting in the negative value of the shear stress along the z-axis. A more detailed discussion of this error has been described in (Yokoyama et al., 2024).

3.2. Impact force

3.2.1. Temporal evolution of impact force

Many studies have focused on the impact force during droplet impact (Zhang et al., 2017; Gordillo et al., 2018; Mitchell et al., 2019a). However, there has been limited investigation into the impact of droplet properties and substrate characteristics on the stress field. A relationship between droplet viscosity and impact force has been found in previous studies, but they only use rigid substrates that do not deform. The effect of substrate elasticity on impact force has not been clarified. However, it is generally difficult to measure pressure in soft substrates using piezoelectric sensors. Piezoelectric sensors are typically effective with hard materials and may have difficulty sensing sufficient pressure in soft materials with large deformation. On the other hand, our stress measurement method can also measure the dynamic stress field in soft substrates during droplet impact. Therefore, it is possible to obtain impact forces by spatially integrating the stress field.

If the substrate deforms, the deformation of the substrate in z-direction can be denoted by $z = \delta(r)$ as a function of radial position r. Since the axial stress acting on the surface of the deformed substrate is $\sigma_{zz}(r, z = \delta(r))$, the impulsive force F acting on the substrate can be estimated by

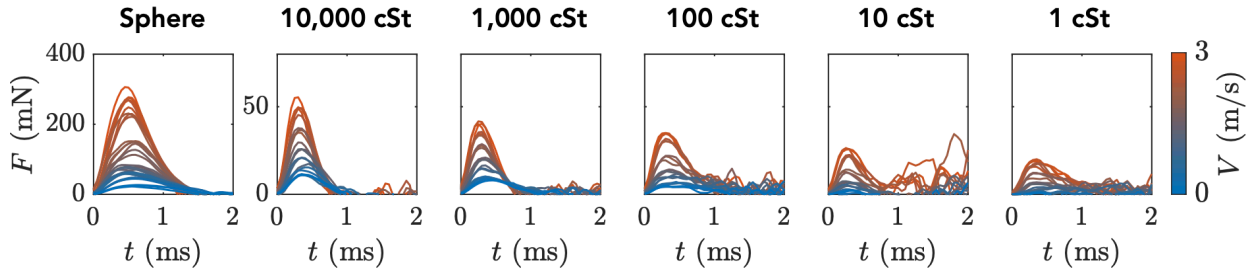

Figure 7. Temporal evolution of impact forces, F, with different impact velocities during a sphere or droplet impact.

integrating the axial stress acting on the substrate surface, i.e.,

$$F = 2\pi \int_0^\infty \sigma_{zz}(r, z = \delta(r))rdr. \tag{18}$$

Fig. 7 shows the temporal evolution of impact force $F(t)$ acting on the surface of the soft substrate during solid sphere or droplet impact. For each droplet impact, the maximum value $F_{\max}$ of the impact force increased with the impact velocity V. This indicates that the impact force increases as the droplet inertia increases. $F_{\max}$ also increased with droplet viscosity η. These trends are similar to the results of previous studies using hard substrates (Zhang et al., 2017; Gordillo et al., 2018).

3.2.2. Scaling law for the maximum impact force

Here, we focus on the maximum impact force $F_{\max}$. We discussed how $F_{\max}$ varies with the impact velocity V, droplet radius R, droplet viscosity η, and substrate elasticity E.

The scaling law for $F_{\max}$ during the impact of a solid sphere, predicted by the Hertzian impact model (Pradipto & Hayakawa, 2021; Kuwabara & Kono, 1987), can be expressed as

$$\tilde{F}_{\max} \propto Ca^{-2/5}. \tag{19}$$

Here, $\tilde{F}_{\max} = F_{\max}/\rho V^2 R^2$ is a dimensionless quantity nondimensionalized by the inertia force of the impactor. The parameter $Ca = \rho V^2/E$ is called the Cauchy number, representing the ratio of droplet inertia force to substrate elastic force. In the case of high-viscous droplets, the scaling law of $\tilde{F}_{\max}$ is expected to show this Hertzian impact scaling. If the droplet viscosity and substrate elasticity are constant, the scaling law can be rewritten as $\tilde{F}_{\max} \propto Re^{-4/5}$, where $Re = \rho VR/\eta$ is Reynolds number. On the other hand, for low-viscosity droplets impacting on a rigid substrate, $F_{\max}$ is proportional to the droplet's inertia force $\rho V^2 R^2$ (Cheng et al., 2022; Soto et al., 2014), resulting in a scaling law of

$$\tilde{F}_{\max} = \text{const}. \tag{20}$$

Fig. 8(a) illustrates the relationship between $\tilde{F}_{\max}$ and Ca. The black dashed line represents the scaling law from Hertzian impact, Eq. (19), and the high-viscous droplet with 10^4 cSt shows a

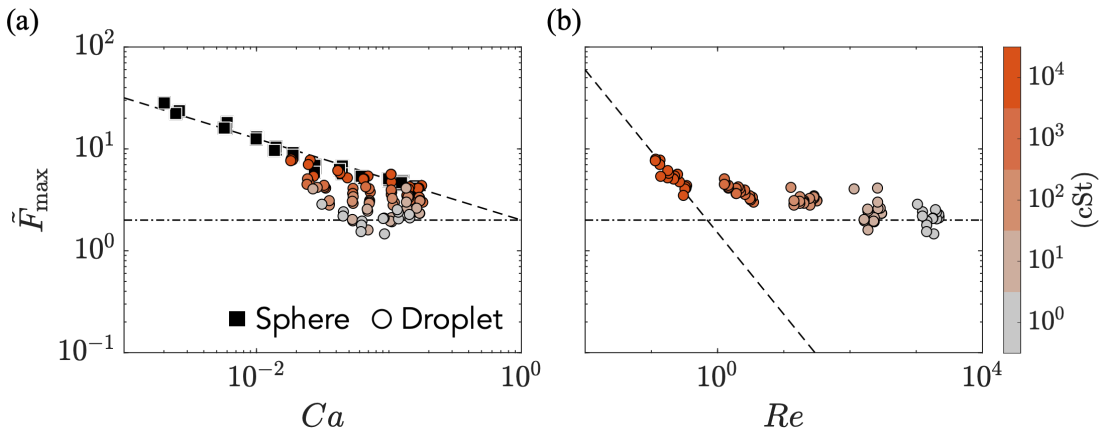

Figure 8. $\tilde{F}_{\max} = F_{\max}/(\rho V^2 R^2)$ v.s. (a) $Ca = \rho V^2/E$ or (b) $Re = \rho V R/\eta$. The black dashed lines indicate the scaling law for the Hertzian impact, $\tilde{F}_{\max} \propto Ca^{-2/5}$. The black dotted-dashed lines indicate the scaling law for inviscid droplet impact on a rigid substrate, $\tilde{F}_{\max} = \text{const.}$

similar trend. As the droplet viscosity decreases, the slope of $\tilde{F}_{\max}$ for each droplet decreases and eventually approaches the scaling law for low-viscous droplet, Eq. (20). To account for the influence of droplet viscosity, Fig. 8(b) shows the results using the Reynolds number on the horizontal axis. Even in this graph, the results for 10^4 cSt droplets show a slope predicted by the scaling law of Hertzian impact, while droplets with decreasing viscosity exhibit different slopes. These results indicate that the crossover of the scaling law for $\tilde{F}_{\max}$ between Eq.(19) and Eq.(20) exists in this region.

3.2.3. Scaling law for the maximum impact force considering the substrate elasticity

Assuming that the maximum force $F_{\max}$ of a droplet colliding with a soft substrate is determined by four physical quantities: ρ, V, R, η, E, Buckingham's Π theorem suggests that $\tilde{F}_{\max}$ can be expressed as a self-similar with Ca and Re as variables, i.e.,

$$\tilde{F}_{\max} = f(Re, Ca). \tag{21}$$

By appropriately combining Re and Ca, it is possible to collapse the data plots of $\tilde{F}_{\max}$ onto a single curve.

Maruoka (2023) proposed a method to find a combination of the dimensionless numbers resulting in data collapse in a parameter range where the scaling laws transition. Initially, a scaling law in a specific limit is defined as a new dimensionless number as Ψ. In this limit, Ψ has a constant value. However, as one approaches the opposite limit, the scaling law transitions, and Ψ deviates from that constant value. The aim of the method is to find a self-similarity parameters which constitutes a self-similar solution to achieve the data collapse.

According to Fig. 8, in the low Re limit, $\tilde{F}_{n\,\max}$ follows the scaling law of Hertzian impact, Eq.

19. Therefore, by defining a new dimensionless number $\Psi = \tilde{F}_{\max}/Ca^{-2/5}$, we assume the folliond self-similar solution, i.e.,

$$\Psi = \Phi(Re \cdot Ca^{\beta}). \tag{22}$$

In the limit of low Re, where it converges to the scaling law of Hertzian impact, $\lim_{Re\to 0} \Psi = \Psi_{\mathrm{Hertz}}$. Thus, the variation in the scaling law with increasing Re is equivalent to the deviation of Ψ from the constant value Ψ_{Hertz}.

In this experiment, by averaging the maximum impact force $F_{\max}$ during solid sphere impact, Ψ_{Hertz} was found to be 1.91. Based on the data-driven method to find the power exponent β resulting in the data collapse of Φ, which was proposed by Maruoka et al. (2024), we found $\beta = -2$, i.e.,

$$\Psi = \Phi\left(Re/Ca^2\right). \tag{23}$$

Fig. 9(a) illustrates a graph with $Z = Re/Ca^2$ on the horizontal axis and Ψ on the vertical axis. For small values of Z, around $Z = 10^1, \Psi$ shows a value close to Ψ_{Hertz}, and as Re/Ca^2 increases, Ψ decreases. The function Φ that captures this trend can be represented, for example, as

$$\Psi = \Phi\left(Z\right) = \Psi_{\mathrm{Hertz}}\left(1 + \frac{Z}{A}\right)^{\kappa}, \tag{24}$$

where A represents the deviation of Ψ from Ψ_{Hertz}, indicating the transition region of the scaling laws, and κ denotes the power exponent of the scaling law in the limit of $Z \gg A$. This function converges to $\Psi = \Psi_{\mathrm{Hertz}}$ in the limit of $Z \ll A$, representing the scaling law of Hertzian impact. On the other hand, in the limit of $Z \gg A$, it converges to a scaling law $\Psi \propto Z^{\kappa}$. The solid line in Fig. 9(a) represents the expression (24) with $A = 10$ and $\kappa = -1/10$, providing a good representation of the trend in the experimental data for Ψ.

Here, let us consider the physical meaning of the combination, $Z = Re/Ca^2$, that provides data collapse for Ψ. Interpreting Re/Ca^2, we have:

$$\frac{Re}{Ca^2} = \frac{R/V}{\eta/E}\frac{E}{\rho V^2} = \frac{\text{Contact time}}{\text{Relaxation time}}\frac{\text{Elastic force}}{\text{Inertial force}}, \tag{25}$$

where η/E represents the relaxation time associated with the deformation of the droplet and substrate surface. On the other hand, R/V represents the time duration in which a droplet contacts with the substrate, namely contact time. Therefore, this combination of dimensionless numbers reflects the ratio between the contact time of droplet and the relaxation time of droplet-substrate deformation, as well as the ratio of substrate elastic force to droplet inertial force. When the contact time is significantly shorter than the relaxation time, an increase in droplet viscosity or a decrease in substrate elasticity suppresses the spreading of the droplet, approaching the scaling law of Hertzian impact. Conversely, when the contact time is longer than the relaxation time, a decrease

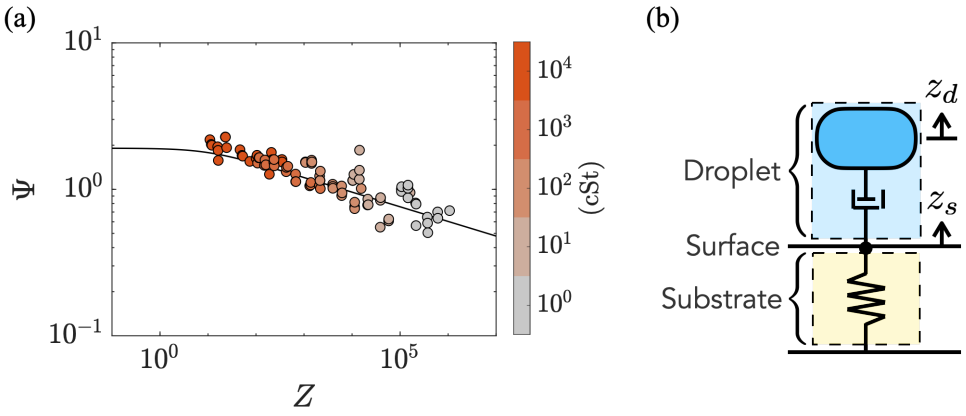

Figure 9. (a) Relationship between $\Psi = \tilde{F}_{\max}/Ca^{-2/5}$ and $Z = Re/Ca^2$. The solid line shows the function of Z, Eq. (24). (b) Mass-dashpot-spring system to model the impact force.

in droplet viscosity or an increase in substrate elasticity accelerates the spreading of the droplet, leading to a deviation from the scaling law of Hertizan impact. This can be considered a key mechanism for determining the maximum impact force of droplets on a soft substrate.

Although we referred to η/E as the "relaxation time," it is traditional to define the relaxation time using the physical properties of the same material. However, it is important to note that η/E we said employs the physical properties of different materials, droplet and substrate. The reason for this can be considered as follows. The droplet and substrate are always in contact from the time of impact until the droplet exhibits maximum impact force. Therefore, the motion of the droplet and substrate can be modeled as a single system then η/E can be adopted as the relaxation time of that system. For instance, if we model this system as a mass-dashpot-spring system consisting of the mass, the viscosity of the droplet, and elasticity of the substrate, as shown in Fig. 9(b), the dimensionless equations of motion regarding the displacement of the surface of the substrate z_s include the ratio of the relaxation time η/E to the contact time R/V.

4. Conclusion

In this study, high-speed photoelastic tomography was employed to quantify dynamic stress fields within a soft substrate during droplet impact. The manuscript outlined the measurement technique, utilizing a high-speed polarization camera and the principles of photoelastic tomography. Using this method, we succeeded in quantitatively measuring the dynamic stress field in a soft substrate during droplet impact. Furthermore, an analysis of the impact force, derived through spatial integration of the measured stress field, was conducted. The discussion delved into the interplay between the maximum impact force, droplet viscosity, and substrate elasticity. As a result, it is indicated that the maximum impact force $F_{\max}$ can be expressed by a function that has a self-similar variable of Re/Ca^2. The combination Re/Ca^2 represents the relationship between

the relaxation time of droplet and substrate deformation, η/E, and the contact time of the droplet, R/V, as well as the ratio of substrate elastic force to droplet inertial force. The maximum impact force $F_{\max}$ can be determined by the balance between the relaxation and contact times.

We believe that our developed method will help to better understand droplet impact phenomena in the future. It may also lead to an understanding of other phenomena related to various engineering processes, such as stress distribution in materials caused by liquid jet impact (Mitchell et al., 2019b) and cavitation bubbles in a viscoelastic material (Rapet et al., 2019).

Acknowledgements

This work was supported by JSPS KAKENHI Grant Numbers JP20H00223, JP22J13343, JP22KJ1239, JP23KJ0859, JP24H00289, JP24KJ2176, and JST PRESTO Grant Number JPMJPR21O5, Japan.

References

Aben, H., Ainola, L., & Errapart, A. (2010a, January). Application of the abel inversion in case of a tensor field. *Inverse Problems in Science and Engineering*, *18*(2), 241–249. doi: 10.1080/17415970903545124

Aben, H., Ainola, L., & Errapart, A. (2010b). Photoelastic tomography as hybrid mechanics. *EPJ Web of Conferences*, *6*, 32009. doi: 10.1051/epjconf/20100632009

Aben, H., Anton, J., & Errapart, A. (2008). Modern photoelasticity for residual stress measurement in glass. *Strain*, *44*(1), 40–48. doi: 10.1111/j.1475-1305.2008.00422.x

Aben, H., & Errapart, A. (2012, October). Photoelastic tomography with linear and non-linear algorithms. *Experimental Mechanics*, *52*(8), 1179–1193. doi: 10.1007/s11340-011-9575-z

Aben, H., & Guillemet, C. (1993). *Photoelasticity of glass*. Berlin, Heidelberg: Springer Berlin Heidelberg. doi: 10.1007/978-3-642-50071-8

Aben, H., & Puro, A. (1997, April). Photoelastic tomography for three-dimensional flow birefringence studies. *Inverse Problems*, *13*(2), 215–221. doi: 10.1088/0266-5611/13/2/002

Aben, H. K., Idnurm, S. J., Josepson, J., Kell, K.-J. E., & Puro, A. E. (1992, November). Optical tomography of the stress tensor field. In *Analytical Methods for Optical Tomography* (Vol. 1843, pp. 220–229). SPIE. doi: 10.1117/12.131894

Anton, J., Errapart, A., Aben, H., & Ainola, L. (2008, October). A discrete algorithm of integrated photoelasticity for axisymmetric problems. *Experimental Mechanics*, *48*(5), 613–620. doi: 10.1007/s11340-008-9121-9

Asai, K., Yoshida, S., Yamada, A., Matsuoka, J., Errapart, A., & Kurkjian, C. R. (2019). Micro-photoelastic evaluation of indentation-induced stress in glass. *Materials Transactions*, *60*(8), 1423–1427. doi: 10.2320/matertrans.MD201903

Breitenbach, J., Roisman, I. V., & Tropea, C. (2018, February). From drop impact physics to spray cooling models: A critical review. *Experiments in Fluids*, *59*(3), 55. doi: 10.1007/s00348-018-2514-3

Cheng, X., Sun, T.-P., & Gordillo, L. (2022). Drop impact dynamics: Impact force and stress distributions. *Annual Review of Fluid Mechanics*, *54*(1), null. doi: 10.1146/annurev-fluid-030321-103941

Dasch, C. J. (1992, March). One-dimensional tomography: A comparison of abel, onion-peeling, and filtered backprojection methods. *Applied Optics*, *31*(8), 1146–1152. doi: 10.1364/AO.31.001146

Doyle, J. F. (1982, January). On a nonlinearity in flow birefringence. *Experimental Mechanics*, *22*(1), 37–38. doi: 10.1007/BF02325702

Errapart, A. (2011). Determination of all stress components of axisymmetric stress state in photoelastic tomography. *Applied Mechanics and Materials*, *70*, 434–439. doi: 10.4028/www.scientific.net/AMM.70.434

Frocht, M. M. (1941). *Photoelasticity: V.1*. John Wiley & Sons Inc.

Gordillo, L., Sun, T.-P., & Cheng, X. (2018, April). Dynamics of drop impact on solid surfaces: Evolution of impact force and self-similar spreading. *Journal of Fluid Mechanics*, *840*, 190–214. doi: 10.1017/jfm.2017.901

Ike, C. C. (2019). Love stress function method for solving axisymmetric elasticity problems of the elastic half-space. *Electronic Journal of Geotechnical Engineering*, *24*(3), 44.

Johnson, K. L. (1985). *Contact mechanics*. Cambridge: Cambridge University Press. doi: 10.1017/CBO9781139171731

Josserand, C., & Thoroddsen, S. (2016). Drop impact on a solid surface. *Annual Review of Fluid Mechanics*, *48*(1), 365–391. doi: 10.1146/annurev-fluid-122414-034401

Kuwabara, G., & Kono, K. (1987, August). Restitution coefficient in a collision between two spheres. *Japanese Journal of Applied Physics*, *26*(8R), 1230. doi: 10.1143/JJAP.26.1230

Liang, G., & Mudawar, I. (2017, March). Review of drop impact on heated walls. *International Journal of Heat and Mass Transfer*, *106*, 103–126. doi: 10.1016/j.ijheatmasstransfer.2016.10.031

Lohse, D. (2022). Fundamental fluid dynamics challenges in inkjet printing. *Annual Review of Fluid Mechanics*, *54*(1), 349–382. doi: 10.1146/annurev-fluid-022321-114001

Love, A. E. H. (1929, January). IX. the stress produced in a semi-infinite solid by pressure on part of the boundary. *Philosophical Transactions of the Royal Society of London. Series A, Containing Papers of a Mathematical or Physical Character*, *228*(659-669), 377–420. doi: 10.1098/rsta.1929.0009

Maruoka, H. (2023, May). A framework for crossover of scaling law as a self-similar solution: Dynamical impact of viscoelastic board. *The European Physical Journal E*, *46*(5), 35. doi: 10.1140/epje/s10189-023-00292-9

Maruoka, H., Yokoyama, Y., & Tagawa, Y. (2024). Data driven method to find... *Under Preparation*.

Mitchell, B. R., Klewicki, J. C., Korkolis, Y. P., & Kinsey, B. L. (2019a, November). Normal impact force of rayleigh jets. *Physical Review Fluids*, *4*(11), 113603. doi: 10.1103/PhysRevFluids.4.113603

Mitchell, B. R., Klewicki, J. C., Korkolis, Y. P., & Kinsey, B. L. (2019b, May). The transient force profile of low-speed droplet impact: Measurements and model. *Journal of Fluid Mechanics*, *867*, 300–322. doi: 10.1017/jfm.2019.141

Miyazaki, Y., Usawa, M., Kawai, S., Yee, J., Muto, M., & Tagawa, Y. (2021, July). Dynamic mechanical interaction between injection liquid and human tissue simulant induced by needle-free injection of a highly focused microjet. *Scientific Reports*, *11*(1), 14544. doi: 10.1038/s41598-021-94018-6

Onuma, T., & Otani, Y. (2014, March). A development of two-dimensional birefringence distribution measurement system with a sampling rate of 1.3mhz. *Optics Communications*, *315*, 69–73. doi: 10.1016/j.optcom.2013.10.086

Otani, Y., Shimada, T., Yoshizawa, T., & Umeda, N. (1994, May). Two-dimensional birefringence measurement using the phase shifting technique. *Optical Engineering*, *33*(5), 1604–1609. doi: 10.1117/12.168435

Philippi, J., Lagrée, P.-Y., & Antkowiak, A. (2016, May). Drop impact on a solid surface: Short-time self-similarity. *Journal of Fluid Mechanics*, *795*, 96–135. doi: 10.1017/jfm.2016.142

Pradipto, & Hayakawa, H. (2021, September). Viscoelastic response of impact process on dense suspensions. *Physics of Fluids*, *33*(9), 093110. doi: 10.1063/5.0061196

Ramesh, K. (2021). *Developments in photoelasticity*. IOP Publishing. doi: 10.1088/978-0-7503-2472-4

Ramesh, K., & Ramakrishnan, V. (2016, December). Digital photoelasticity of glass: A comprehensive review. *Optics and Lasers in Engineering*, *87*, 59–74. doi: 10.1016/j.optlaseng.2016.03.017

Rapet, J., Tagawa, Y., & Ohl, C. D. (2019, March). Shear-wave generation from cavitation in soft solids. *Applied Physics Letters*, *114*(12), 123702. doi: 10.1063/1.5083141

Soto, D., Larivière, A. B. D., Boutillon, X., Clanet, C., & Quéré, D. (2014, June). The force of impacting rain. *Soft Matter*, *10*(27), 4929–4934. doi: 10.1039/C4SM00513A

Sun, T.-P., Álvarez-Novoa, F., Andrade, K., Gutiérrez, P., Gordillo, L., & Cheng, X. (2022, March). Stress distribution and surface shock wave of drop impact. *Nature Communications*, *13*(1), 1703. doi: 10.1038/s41467-022-29345-x

Sun, Y., Zheng, Y., Liu, C., Zhang, Y., Wen, S., Song, L., & Zhao, M. (2022, May). Liquid marbles, floating droplets: Preparations, properties, operations and applications. *RSC Advances*, *12*(24), 15296–15315. doi: 10.1039/D2RA00735E

Xiong, Y., Huang, H., & Lu, X.-Y. (2020, May). Numerical study of droplet impact on a flexible substrate. *Physical Review E*, *101*(5), 053107. doi: 10.1103/PhysRevE.101.053107

Yarin, A. (2006). Drop impact dynamics: Splashing, spreading, receding, bouncing.... *Annual Review of Fluid Mechanics*, *38*(1), 159–192. doi: 10.1146/annurev.fluid.38.050304.092144

Yokoyama, Y., Ichihara, S., & Tagawa, Y. (2024, July). High-speed photoelastic tomography for axisymmetric stress fields in a soft material: Temporal evolution of all stress components. *Optics and Lasers in Engineering*, *178*, 108224. doi: 10.1016/j.optlaseng.2024.108224

Yokoyama, Y., Mitchell, B. R., Nassiri, A., Kinsey, B. L., Korkolis, Y. P., & Tagawa, Y. (2023, February). Integrated photoelasticity in a soft material: Phase retardation, azimuthal angle, and stress-optic coefficient. *Optics and Lasers in Engineering*, *161*, 107335. doi: 10.1016/j.optlaseng.2022.107335

Zhang, B., Li, J., Guo, P., & Lv, Q. (2017, August). Experimental studies on the effect of reynolds and weber numbers on the impact forces of low-speed droplets colliding with a solid surface. *Experiments in Fluids*, *58*(9), 125. doi: 10.1007/s00348-017-2413-z